Atomistic study on dislocation emission from segregated grain boundaries in high-entropy alloys

Kohei Shiotani *
Division of Mechanical Science and Engineering, Graduate School of Natural Science and Technology, Kanazawa University, Kakuma-machi, Kanazawa, Ishikawa 920-1192, Japan

Tomoaki Niiyama and Tomotsugu Shimokawa †
Faculty of Mechanical Engineering, Institute of Science and Engineering, Kanazawa University, Kakuma-machi, Kanazawa, Ishikawa 920-1192, Japan

(Received 2 March 2023; accepted 5 December 2023; published 27 December 2023)

As one of the promising candidates for developing next-generation structural materials, high-entropy alloys (HEAs) have recently attracted significant interest because of their unique mechanical properties, including their coexisting of high strength and ductility properties. Here, through atomic simulations, we demonstrate that the segregation of elements to grain boundaries (GBs) due to atomic-size differences, which is one of the most important characteristics of HEAs, contributes to the coexistence of high strength and high ductility in HEAs. To focus on only the effect of the size difference on the GB segregation, ignoring the difference in the chemical bonding energies among all the constituent elements, we employ two-dimensional virtual quinary HEA models. The HEAs are subjected to tensile and compressive load tests, and the stress required for dislocation emission from the GBs is measured. We demonstrate that the GB segregation in the HEAs increases the stress required for dislocation emission from the GBs, thereby increasing the strength of the HEAs. This is because the GB segregation in the HEAs stabilizes the GB structure by decreasing the GB free volume. Notably, the GB segregation also decreases the heterogeneity of the mechanical field between the grain interiors and the GBs, which is an intrinsic attribute of ordinary materials, and the homogenization of the mechanical field can improve the ductility of HEAs, preventing intergranular fracture. Our results can serve as a guide for designing HEAs with both high strength and high ductility through the effective utilization of GB segregation.

DOI: 10.1103/PhysRevMaterials.7.123606

I. INTRODUCTION

High-entropy alloys (HEAs) [1,2] are crystalline metallic materials composed of five or more elements in near-equal atomic percentages (at. %). Recently, they have been attracting significant attention because of their various unique mechanical properties; for example, they exhibit high strength and high toughness simultaneously [3–5], high-temperature strength [6,7], and superior fatigue behavior [8,9]. Therefore HEAs hold incredible application potential and are expected to be widely employed in the development of next-generation structural materials [10–12].

One of the characteristics of HEAs is the atomic-size differences among the constituent elements. This size difference induces the atomic-scale heterogeneity of the mechanical field in the lattice [10,11,13] and is considered to be strongly related to the excellent mechanical properties of HEAs [14–19]. Okamoto *et al.* [20] reported that a CrMnFeCoNi HEA (called the Cantor alloy [1]) and its subsets established a positive correlation between the magnitude of lattice distortion and the yield stress, indicating that lattice distortion essentially serves as an obstacle to the dislocation glide [21]. Therefore the strength of HEAs can be improved simply by combining elements with different atomic sizes, even without any obstacles to the dislocation motion, such as solute atoms or precipitates, which generally strengthen conventional dilute alloys.

The atomic-size difference may also affect the stability of the grain boundaries (GBs) in HEAs. Generally, GBs are interfaces between adjacent grains with different crystallographic orientations, where the translational symmetry of the crystal lattice is broken. The GB structure results in relatively high energy and an excess atomic free volume [22,23], inducing the grain-size-scale heterogeneity of the mechanical field in polycrystalline materials. Thus GBs contribute significantly to the inelastic phenomena, e.g., diffusion [24], dislocation sources and sinks [25], dislocation motion [26], and fracture [27]. Notably, GB segregation in HEAs decreases the GB excess energy and atomic free volume. Therefore, by forming GBs with elements having atomic sizes that compensate for the atomic free volume at the GBs, i.e., if large atoms can segregate to large spaces and vice versa, the stability of GBs in HEAs can be improved. Consequently, the grain-size-scale heterogeneity that is observed in ordinary materials can be expected to disappear due to GB segregation. In other words, the mechanical field of the GBs in the segregated HEAs exhibiting only atomic-scale heterogeneity is expected to influence their various unique mechanical properties [3–9]. Recently, many experimental techniques, such as atom probe

*k.shiotani@stu.kanazawa-u.ac.jp
†simokawa@se.kanazawa-u.ac.jp

tomography, have confirmed elemental GB segregation in HEAs [28–33]. However, it is difficult to elucidate the relationship between GB segregation and the mechanical properties of HEAs using only experimental approaches.

Atomic simulations are highly valuable for investigating the influence of the GB structure on GB-mediated plasticity. Recently, molecular dynamics (MD) analyses have shown the importance of controlling the active slip systems at GBs by designing the GB structure, which considerably influences the critical resolved shear stress (CRSS), improving the ductility and fracture toughness of ultrafine-grained and nanocrystalline metals [27,34]. For HEAs, significant aspects of GB segregation, such as elemental segregation to GBs [35], GB migration [36], dislocation emission [37], and tensile strength [38] have recently been investigated by atomic simulations. However, the influence of the segregated GB structure on GB-mediated plasticity remains unclarified. If the GB segregation changes the relationship between the GB energy and the GB structure, the GB-mediated plastic deformation mechanisms, i.e., the active slip systems for the segregated GBs, may differ from those for non-GB-segregated HEAs. Therefore the role of GB segregation in GB-mediated plasticity should be elucidated to develop design guidelines for HEAs. Here, notably, one of the reasons why the relationship between the GB segregation and the plasticity phenomena in HEA has not been clarified is the complexity of the GB segregation phenomenon. In addition to atomic-size differences, there are differences in binding energies between elements. Therefore one way to understand this phenomenon in detail is to separate the effects of the atomic-size differences from those of the bonding-energy differences.

In this study, we systematically investigate the effects of GB segregation caused by atomic-size differences on dislocation emission from the GBs in HEAs using atomistic simulation methods based mainly on MD. To clarify the effect of the atomic-size difference on the GB segregation, ignoring the effect of chemical interaction forces, we employed two-dimensional virtual quinary HEA models, in which the bonding energies among all the atoms are equivalent and only the atomic sizes of the elements are different. Furthermore, to clarify the influence of the GB segregation on the dislocation emission, 12 kinds of symmetrical tilt GBs are adopted because the effects of the GB structure on the dislocation emission are well understood in single-element materials [25,39–41]. First, we perform GB-segregation simulations at different temperatures using a combination of Monte Carlo (MC) and MD methods for various symmetric tilt GBs, and we obtain approximately 300 bicrystal models (6 temperatures, 4 atomic-size differences, and 12 GBs). Second, the relationship between the GB segregation and the GB free volume is investigated, after which the influence of the GB segregation on the CRSS required for dislocation emission from the GBs is examined by performing tensile and compressive load tests. Finally, we discuss the GB-segregation-induced homogenization of the mechanical field around the GB regions and the influence of the segregation on the GB-structure dependence of the activated slip systems.

II. METHOD

A. Two-dimensional modeling of quinary HEAs

1. Modeling overview

Attractive mechanical properties of HEAs are complexly related to a variety of factors, such as the number of constituent elements, element combinations, atomic-size differences, and chemical binding energies between different elements [10–12]; therefore, the modeling of HEAs is very important to identify dominant factors. In general, there are two approaches to modeling in atomic simulation: one is realistic modeling that considers all candidate factors, and the other is simplified modeling that considers only selected candidate factors. The advantage of the former approach is to express the synergistic effect due to the interaction of each factor, while the disadvantage is that it is difficult to decompose the contribution of each factor. On the other hand, the advantage of the latter approach is that the contribution of each factor can be clarified although the synergistic effect cannot be observed.

The dislocation emission from the segregated GB in HEAs, which is the target in this study, is one of the most complex phenomena involving various factors. GB segregation is expected to be strongly caused by atomic-size differences and chemical bonding energies between different elements, while dislocation emission from GBs is supposed to be strongly affected by GB free volume and GB structure. GB segregation is predicted to affect GB free volume and GB structure. Therefore it is important to understand how the atomic-size difference and the chemical bonding forces each influence the dislocation emission from segregated GBs, leading to an understanding of the mechanisms by which the mechanical properties of HEA are manifested. In this study, based on the latter approach with simplified modeling, we focus only on the impact of the atomic-size difference on the dislocation emission from segregated GBs in HEAs using virtual quinary HEA models of a two-dimensional triangular lattice with various atomic-size differences but equal binding energies between different elements.

2. Interatomic interactions

To investigate the effect of the atomic-size difference on the GB segregation, ignoring the effect of chemical interaction forces, a shifted-force Morse (SFM) potential [42] $\phi_s(r)$, based on the Morse potential [43] $\phi(r)$, is adopted to represent the atomic interaction in the virtual quinary HEA models. The use of the SFM potential enables to achieve conservation of the total energy of atomic systems while improving the efficiency of computation time by introducing a cutoff distance and reducing the interaction energy and its derivative (the interaction force) to zero at the cutoff distance. The advantage of the simple interatomic potential is that it enables the design of virtual HEAs having the same interatomic forces but different atomic-size differences by tuning a few parameters. Further, it facilitates the systematic investigation of the influence of the atomic-size difference on the GB segregation. Understandably, currently, it is not easy to conduct such a systematic

study by assembling realistic interatomic potentials of actual HEAs [38,44–48]. We have reported the applicability of this simple potential through the investigation of the atomic-size difference dependence of GB mediated plastic phenomena in multicomponent alloys [37].

The Morse potential is described as follows:

$$\phi(r) = D^{ij}\{e^{-2\alpha^{ij}(r-r_0^{ij})} - 2e^{-\alpha^{ij}(r-r_0^{ij})}\}, \tag{1}$$

where parameters D^{ij}, α^{ij}, and r_0^{ij} correspond to the cohesive energy, elastic constants, and equilibrium distance between elements i and j, respectively. A SFM potential, $\phi_s(r)$ is constructed by tuning a two-body interatomic potential function, $\phi(r)$, as follows:

$$\phi_s(r) = \begin{cases} \phi(r) - \phi(r_c) - (r - r_c)\frac{d\phi(r_c)}{dr} & (r \leqslant r_c) \\ 0 & (r > r_c) \end{cases}, \tag{2}$$

where r_c is the cutoff distance. Since the HEAs in this study are quinary systems, we represent elements i and j by integers from 1 to 5. The virtual HEAs are composed of elements with variable geometrical effects, such as interatomic distances, but invariable chemical effects, such as interatomic bonds. The HEAs can be represented by tuning the parameter relevant to the atomic sizes and maintaining as constants the parameters relevant to the cohesive energy and elastic constants, as follows:

$$\begin{aligned} D^{ij} &= D = 4.331 \times 10^{-20}\ \text{J} \\ \alpha^{ij} &= \alpha = 11.65\ \text{nm}^{-1} \\ r_0^{ii} &= r_0^{33} + (i-3)R, \end{aligned} \tag{3}$$

where $R = \eta(k-1)$, $r_0^{33} = 0.3253$ nm, $\eta = 5 \times 10^{-4}$ nm, and $k = 1, 2, \ldots, 5$, respectively. The r_0^{ij} between different elements, i and j is given as $r_0^{ij} = (r_0^{ii} + r_0^{jj})/2$. The parameter, k changes the atomic-size difference of the constituent elements and is required as many as the atomic-size difference parameter δ, defined by the following equation [49]:

$$\delta = 100\sqrt{\sum_{i=1}^{n}\left(1 - \frac{a_i}{\sum_{j=1}^{n} c_j a_j}\right)^2}, \tag{4}$$

where n is the number of constituent elements, and c_i and a_i represent the mole fraction and atomic size of element i, respectively. In this study, the values are set in the range of $\delta = 0$–2.28, where the crystal structures are stabilized in two-dimensional models [37] and actual three-dimensional HEAs [10]. In other words, the atomic-size differences of the HEA models in this study are realistic values. Figure 1 shows the size of the constituent elements producing each atomic-size difference, δ. As one can see clearly, the size difference between the smallest and the largest elements in each δ increases with δ. The cutoff distance is set as $r_c = 0.8$ nm for all the atomic pairs. We referred to the parameters of the Morse potential developed by Girifalco *et al.* [50] based on the experimental data of Al: $D = 4.331 \times 10^{-20}$ J, $\alpha = 11.65\ \text{nm}^{-1}$, and $r_0 = 0.3253$ nm. By determining the potential parameters based on Al, we can construct virtual HEAs with high ductility similar to that of Al.

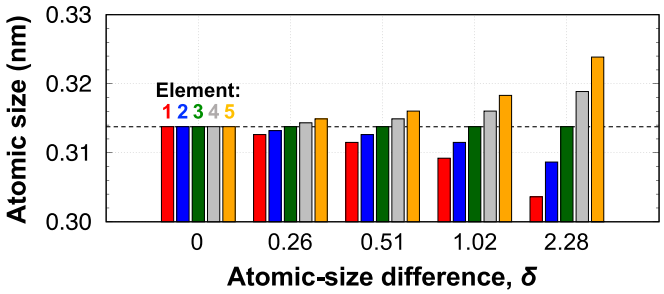

FIG. 1. The size of the constituent elements belonging to each atomic-size difference, δ. Note that the size of each element is obtained by relaxation calculations of the single-element materials.

3. Bicrystal models

In this study, 12 kinds of symmetric tilt GBs are analyzed. The GBs are created by constructing two separate crystals composed of regular triangular lattices with the desired crystallographic orientation angle, $\pm\theta/2$, and joining them along a plane normal to the y axis [51] (see Fig. 2). The interface between the two crystals is the GB. In a two-dimensional bicrystal model with a triangular lattice, the GB orientation angle is in the range of $0 \leqslant \theta \leqslant 60^\circ$ First, to obtain a GB structure with no lattice distortion, we prepared a bicrystal model with a single-element material ($\delta = 0$) in which the atomic sizes are the same for all elements. Depending on the atomic-scale translational displacement of the two grains along a direction parallel to the GBs, the GBs may have different structures and energies even if the grains have the same orientation angle, θ [52]. In this study, the GB structure with the minimum energy in each θ is adopted. After determining the most stable GB structure in the single-element materials, bicrystal models of HEAs ($\delta \neq 0$) are created by randomly replacing the atoms with five different constituent atoms with equal atomic percentages. Depending on the GB orientation angle, the sizes of the bicrystal models may differ. The lengths parallel and perpendicular to the GB are in the ranges of 21–24 nm and 10–19 nm, respectively, and the total number of atoms is in the range of 2500–5000.

Figures 2(a)–2(d) show the atomic structures of the four kinds of GBs in the single-element materials ($\delta = 0$). We use the centrosymmetry parameter (CSP) [53] to distinguish between the atoms within the crystalline region and those within the GB region. The atoms with a CSP value higher than 0.3 are colored white and are in the GB region. In three-dimensional atomic models, it has been reported that symmetric tilt GBs are represented by periodically arranged GB structural units [25,41,54]. In the two-dimensional triangular lattice system, four types of structural units can be observed: A, B, C, and D, which represent the GB structure from $\theta = 0^\circ$–60°. The A structural unit can express the single crystal structure with $\theta = 0^\circ$ and the combination of the structural units, B and D can express the single crystal structure with $\theta = 60^\circ$ The GB structures with an angle between these two angles can be expressed by the combination of these three structural units and the structural unit C having a square shape.

Figure 2(e) shows the GB energy, γ_{GB}, in the single-element materials ($\delta = 0$) at 1 K, as a function of the GB misorientation angle θ. The GB energy is calculated by the

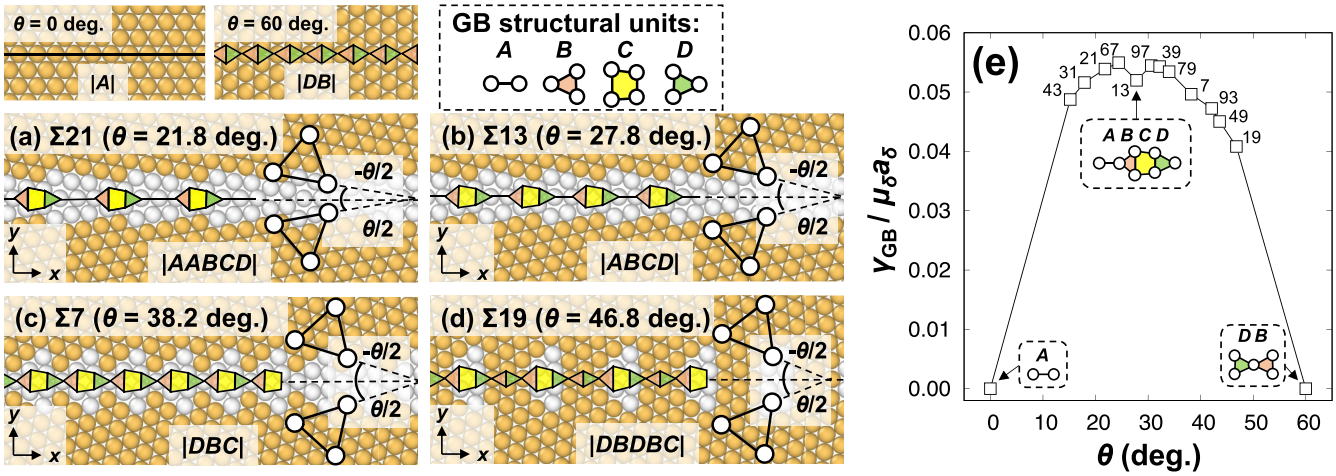

FIG. 2. Atomic structures around the (a) Σ21 ($\theta = 21.8°$), (b) Σ13 ($\theta = 27.8°$), (c) Σ7 ($\theta = 38.2°$), and (d) Σ19 ($\theta = 46.8°$) boundary for a single-element material ($\delta = 0$), as examples of the initial atomic configuration with symmetrical tilt GBs created by rotating two grains by $\pm\theta/2$ (deg.). The atoms are classified according to centrosymmetry parameter (CSP) values [53]. If the value of an atom is CSP > 0.3, the atom is considered to be within the GB regions and is colored white. The GB structural units defined in this study, *A*, *B*, *C*, and *D*, are outlined. The structural unit, *A* is from a single crystal at $\theta = 0°$, whereas *B* and *D* are from that at $\theta = 60°$ The four kinds of GBs shown in this figure are created by the combination of the four structural units. (e) GB energy, γ_{GB}, as a function of the misorientation angle, θ for single-element materials ($\delta = 0$). γ_{GB} is normalized by the shear modulus for $\delta = 0$, μ_δ, and a_δ. The Σ values are represented according to the misorientation angle.

following equation:

$$\gamma_{GB} = \frac{1}{A_{GB}}\left(E_{tot} - \frac{N_{tot}}{N_{PC}}E_{PC}\right), \tag{5}$$

where A_{GB}, E, and N are the GB area, potential energy, and the number of atoms in the whole system, respectively. Subscripts "tot" and "PC" of E and N indicate that the values are for a system including the GBs and a perfect crystal, respectively. We define the GB area in the two-dimensional systems as $A_{GB} = l_x a_\delta$, where l_x and a_δ are the lengths of the systems parallel to the x-axis and normal to the xy plane (the same as the lattice constant), respectively. Note that a_δ is introduced as a "thickness" of the models to evaluate "area" and "volume" in the present two-dimensional models. In this study, normalizing quantities including the length, e.g., GB free volume and energy, by a_δ to avoid the ambiguity in the definition of the thickness, we will concentrate on the relative relationship of the quantities relating to mechanical properties rather than the absolute values of those. The GB energy shown in Fig. 2(e) is normalized by a shear modulus, μ_δ, and a lattice constant, a_δ, in a single crystal at $\delta = 0$. The GB energy increases with the misorientation angle from the single crystals ($\theta = 0°$ or 60°) and reaches the maximum around $\theta = 30°$. For two-dimensional symmetric tilt GBs, the Σ13 boundaries, whose misorientation angles are near $\theta = 30°$, show an energy cusp. Generally, in the GBs in the three-dimensional models, the large-angle boundary exhibits the maximum GB energy, and energy cusps can be observed at some GB misorientation angles depending on the simple combination of the structural units [22,41,54–59]. Therefore, even the GBs with two-dimensional models here can capture the characteristics of general GBs, enabling the qualitative analysis of the dependence of the GB structure on the dislocation emission from the GBs.

4. Relaxation to the thermally equilibrated structures of HEAs

After creating the bicrystal models including the symmetric tilt GBs, we determine the thermally equilibrated atomic configuration using a combination of MD and MC methods, as described below.

First, two atoms are randomly selected, and their positions are swapped. After the atom swap, a structural relaxation calculation with time integration of 2 fs/step is performed 50 times [60] at 1 K to evaluate the potential-energy difference in the whole system before and after the atom swap, ΔE. If $\Delta E \leqslant 0$, the atom swap is accepted, otherwise the acceptance of the swap is subject to the Metropolis criterion [42], $\exp[-\Delta E/(k_B T_a)]$, where k_B and T_a are the Boltzmann constant and the annealing temperature, respectively. The number of trials of the swap (MC step) is 10^5. When T_a is small, the atom swaps with comparatively low ΔE values are preferentially accepted so that certain elements that decrease the GB energy can gather at the GBs, resulting in GB segregation.

Periodic boundary conditions are applied in all directions during the simulations, and the velocity scaling method [42] is employed to control the temperature during the structural relaxation calculations. Furthermore, the Parrinello-Rahman method [61] is employed to adjust the normal stresses in the analysis models to zero by changing the size of the simulation cell. The annealing temperature, T_a, associated with the acceptance or rejection of the atom swaps at MC is $T_a = 0.001\ T_m$, $0.1\ T_m$, $0.3\ T_m$, $0.5\ T_m$, and $0.7\ T_m$, where $T_m = 1032.8 \pm 7.4$ K is the average melting point of the single crystals of δ =0–2.28, and it is calculated from 10 HEA samples, in which each element is randomly distributed on the crystal lattice in each δ. In this study, the HEAs with and without the aforementioned hybrid MD/MC procedure are denoted as "annealed HEAs" and "random HEAs,"

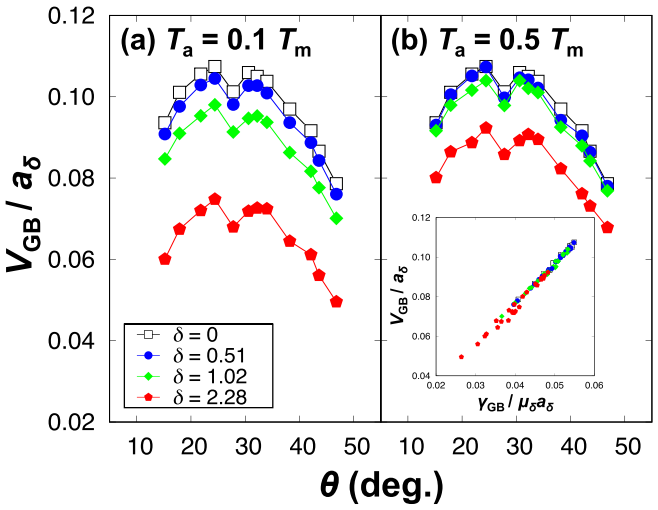

FIG. 3. Grain boundary free volume, V_{GB}, as a function of the misorientation angle, θ, for single-element materials ($\delta = 0$) and the annealed HEAs ($\delta \neq 0$) at (a) $T_a = 0.1\ T_m$, and (b) $T_a = 0.5\ T_m$, respectively. V_{GB} is divided by a lattice constant, a_δ, in each δ. The inset shows the correlation between the GB energy,γ_{GB}, and V_{GB}. γ_{GB} is also normalized by the shear modulus, μ_δ, and a_δ in each δ.

respectively. It should be noted that two GBs exist in each analysis model by applying the periodic boundary conditions.

B. Tensile and compressive load tests

For the annealed HEAs and the random HEAs obtained by the method above, structural relaxation calculations for 50 ps, followed by tensile/compressive load tests at a strain rate of $|\dot{\varepsilon}| = 1 \times 10^8\ s^{-1}$ with a temperature of 1 K are conducted for the two analyses: One is the stress for the first dislocation emission from either of the two GBs (Sec. III 2) and the other development of mechanical fields around the GBs before the first dislocation emission from either of the two GBs (Sec. IV 1). During the analyses, the periodic boundary conditions and the control of temperature and stress are implemented in the same way as in the modeling methods described above.

As described above, the HEAs in this study are created with a combination of 12 kinds of GBs, 4 kinds of atomic-size differences, and 6 kinds of annealed temperatures; therefore, 288 HEAs are prepared for the analyses of the dislocation emission from the GBs. OVITO [62] is employed for visualizing the atomic structure and for post-analysis after the MD calculations.

III. RESULTS

A. Segregation effects on the grain boundaries in HEAs

1. Grain boundary free volume

Figure 3 shows the relationship between the GB free volume V_{GB}, and the GB misorientation angle, θ, in the annealed HEAs at a temperature of T_a. The GB free volume is calculated as follows:

$$V_{GB} = \frac{1}{A_{GB}}\left(V_{tot} - \frac{N_{tot}}{N_{PC}}V_{PC}\right), \tag{6}$$

where V_{tot} and V_{PC} are the volumes of the simulation cell with and without GBs, respectively. The GB free volume shown in Fig. 3 is normalized by the lattice constant, a_δ in each δ. The inset figure shows the correlationship between the GB free volume and GB energy, γ_{GB}, normalized by shear modulus, μ_δ and a_δ in each δ.

In the relationship between θ and V_{GB} at $T_a = 0.1\ T_m$, the GB free volume decreases with an increase in δ at each misorientation angle, suggesting that the intrinsic atomic free volumes at the GBs, which are individual to the GB structure, decrease with an increase in δ. A similar trend can be observed at $T_a = 0.5\ T_m$. In the θ–V_{GB} relation at $\delta = 2.28$, the GB free volume decreases with T_a. The trend appears to be more pronounced as δ increases. The decrease in the GB free volume in the HEAs indicates the emergence of atomic-scale heterogeneity in the grain interiors caused by the atomic-size difference and that the grain-size-scale heterogeneity of the mechanical field is reduced.

From the inset of Fig. 3, we can confirm a strong correlation between the GB energy and the GB free volume. The positive correlation has been previously reported from three-dimensional MD calculations [22,55–59,63–65] and first-principles calculations [23,66]. Therefore, similar to the GB free volume, the GB energy also decreases with an increase in δ or a decrease in T_a. It should be noted that there is no guarantee that the positive correlation will hold at segregated grain boundaries in multiple HEA systems, because the grain boundary free volume may remain unchanged even if atomic pairs with strong chemical binding energy segregates at the grain boundary and the grain boundary energy is reduced. The inset in Fig. 3 shows a strong linear relationship between the grain boundary free volume and its energy even if grain-boundary segregation occurs especially at low temperatures. This result indicates that we have successfully modeled HEAs with no difference in interaction energy between different elements.

2. GB composition and GB free volume

To investigate the effect of the GB segregation on the GB free volume, Fig. 4(a) shows the distribution of the atomic volume, V_a, around the $\Sigma 13$ boundary of the single-element material ($\delta = 0$). V_a is calculated using the Voronoi tessellation method by OVITO [67]. We define the length normal to the xy plane (the same as the lattice constant) as a_δ; this is also applied in the calculation of the GB energy or the GB free volume. The atoms constituting the GB structural units are numbered in ascending order of the atomic volume. We can confirm that the atoms within the GB region have different atomic volumes according to their accommodation sites. Figures 4(b)–4(d) show the elemental distribution around the $\Sigma 13$ boundary in the HEAs ($\delta \neq 0$) annealed at various temperatures, T_a. At the GB at $\delta = 0.51$ and $T_a = 0.001\ T_m$ shown in Fig. 4(b), the largest element (element 5) occupies the largest accommodation site and vice versa. This suggests that GB segregation occurs. In the GB at $\delta = 0.51$ and $T_a = 0.3\ T_m$ shown in Fig. 4(c) or the GB at $\delta = 2.28 T_a = 0.3\ T_m$ in Fig. 4(d), we cannot visually confirm the GB segregation.

To quantitatively investigate the degree of GB segregation, Figs. 5(a)–5(c) show the relationship between the elemental

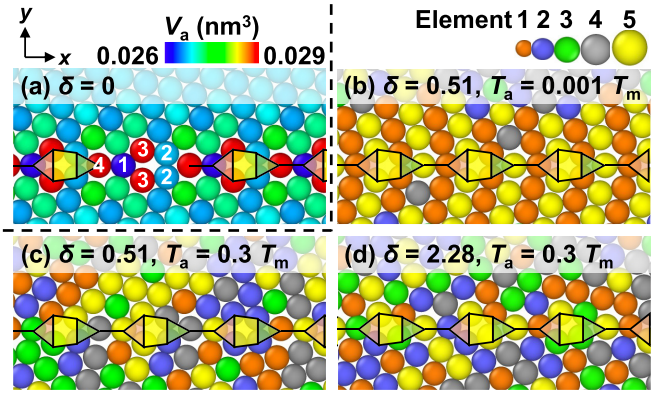

FIG. 4. (a) Distribution of the Voronoi atomic volume [67], V_a, around the Σ13 boundaries in the single-element materials ($\delta = 0$). The atoms constituting the GB structural units are numbered in ascending order of the atomic volume. [(b)–(d)] Distribution of each element around the GBs at different δ and T_a.

composition at the GBs, c_i^{GB} (element; $i = 1, 2, \ldots, 5$) and the GB misorientation angle, θ. If the GBs have no compositional deviations, $c_i^{GB} = 0.2$ since the HEAs in this study have equimolar compositions. If the annealing temperature is different under a constant δ, as shown in Figs. 5(a) and 5(b), two kinds of elements (elements 1 and 5) segregate to the GBs at low temperatures. If δ is different under a constant annealing temperature, as shown in Figs. 5(b) and 5(c), the degree of the GB segregation increases with the δ. value. From the two results, it is clear that the degree of GB segregation increases with an increase in δ and a decrease in the annealing temperatures. A similar trend was confirmed in the GB free volume, suggesting a correlation between the GB free volume and the degree of GB segregation.

To quantitatively investigate the relationship between the GB segregation and the GB free volume, we define a parameter, Δc, as follows:

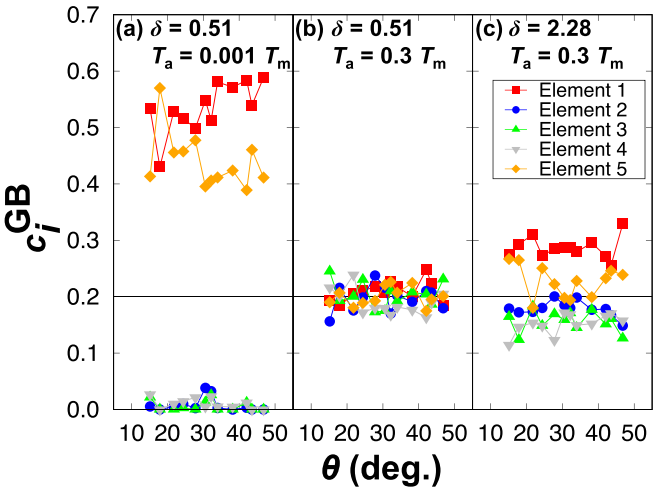

FIG. 5. Atomic composition of element i at GBs, c_i^{GB}, as a function of misorientation angle, θ, at (a) $\delta = 0.51$, $T_a = 0.001\ T_m$, (b) $\delta = 0.51$, $T_a = 0.3\ T_m$, and (c) $\delta = 2.28$, $T_a = 0.3\ T_m$, respectively.

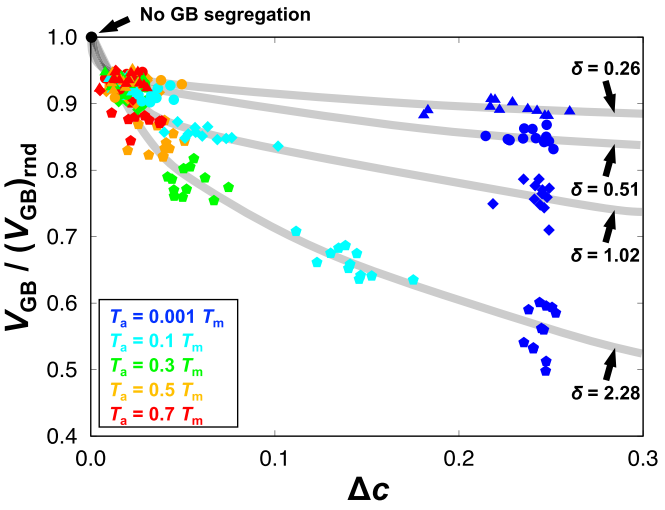

FIG. 6. Relationship between the GB free volume, V_{GB}, normalized by the GB free volume of random HEAs and the standard deviation of the GB atomic compositions, Δc. The curved lines are visual guides for each δ.

$$\Delta c = \sqrt{\frac{1}{n}\sum_{i=1}^{n}\left(c_i^{GB} - c_i\right)^2}, \tag{7}$$

where n is the number of the constituent elements in the HEAs ($n = 5$ in this study) and c_i^{GB} and c_i are the concentrations of element i at the GBs and in the whole system, respectively. Therefore Δc represents the standard deviation of the GB composition. Figure 6 shows the relationship between the GB free volume, V_{GB} and the degree of GB segregation, Δc. V_{GB} is normalized by the GB free volume in random HEAs. When no GB segregation occurs, we can obtain $\Delta c = 0$ and $V_{GB}/(V_{GB})_{rnd} = 1$ from the definitions of these parameters. The gray curves in the figure are visual guides for the easy understanding of the relations between Δc and $V_{GB}/(V_{GB})_{rnd}$ in each δ. As described in the figure, $V_{GB}/(V_{GB})_{rnd}$ decreases with an increase in Δc at all δ values, suggesting that the GB segregation decreases the intrinsic atomic free volumes at the GBs. The decreasing trend of $V_{GB}/(V_{GB})_{rnd}$ with an increase in Δc becomes more pronounced as δ increases. This indicates that HEAs with large atomic-size differences experience significant GB segregation, which decreases the GB free volume. In the model HEAs, the temperature regimes in which strong degree of GB segregation occurs are lower than 0.3 T_m and are also lower as a practical temperature such as ~0.6 T_m. This indicates that the driving force for grain boundary segregation due to the atomic-size differences is very small and the other factors, such as mixing enthalpy related to the chemical bonding energies between different elements, are necessary for grain boundary segregation at higher temperatures to be feasible in actual HEAs.

In Sec. III 1, we discuss the characteristics of GBs in annealed HEAs. The GB free volume decreases with the annealing temperature or with an increase in the atomic-size difference. The GB segregation contributes to the decrease in the GB free volume. The decrease in the GB free volume in

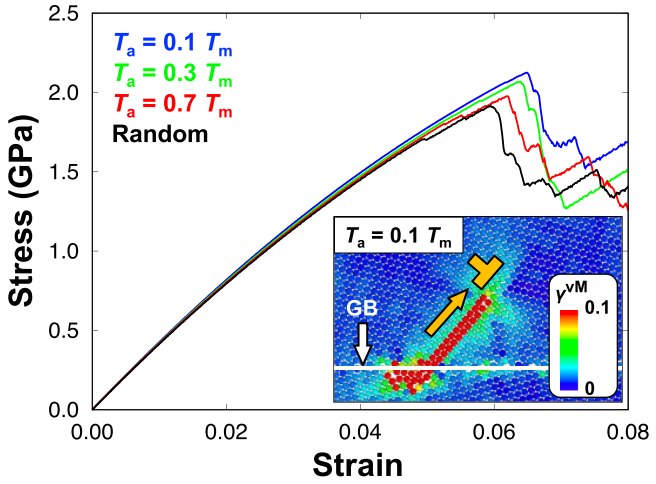

FIG. 7. Stress-strain curves for the $\Sigma13(\theta = 27.8^\circ)$ boundaries at $\delta = 2.28$. The stress decreases sharply when the dislocation is emitted from the GBs. The inset figure shows the dislocation emission from the $\Sigma13$ boundary with the thermal equilibrium configuration at $T_a = 0.1\ T_m$. The atoms are colored according to the atomic von Mises strain [68], γ^{vM}.

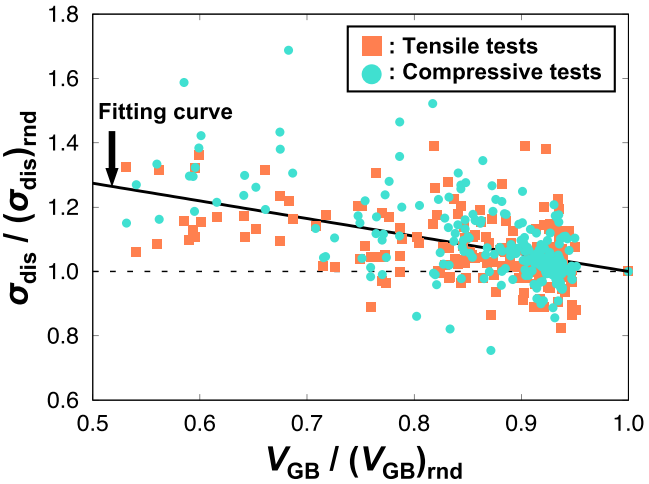

FIG. 8. Relationship between the normalized dislocation emission stress from the GBs and the normalized GB free volume.

the HEAs indicates the occurrence of the atomic-scale heterogeneity in the grain interiors caused by the atomic-size difference and that the grain-size-scale heterogeneity of the mechanical field is reduced. In Sec. III 2, we discuss the roles of GB segregation on dislocation emission from GBs in HEAs.

B. Segregation effects on dislocation emission from grain boundaries in HEAs

Figure 7 shows the tensile stress-strain curves for the HEAs with $\Sigma13$ boundaries at $\delta = 2.28$, where the black solid curve is obtained from the random HEA, and the blue, green, and red curves are the results of the annealed HEAs at $T_a = 0.1\ T_m$, $0.3\ T_m$, and $0.7\ T_m$, respectively. In the curves, we can observe sharp stress drops at strains of 0.06–0.07, where the dislocation emission from the GBs occurs. The inset figure shows a snapshot of the dislocation emission from the GB in the HEA annealed at $T_a = 0.1\ T_m$. Atoms are colored according to the atomic von Mises strain [68], γ^{vM}. The stress-strain curves show that the stress required for dislocation emission increases with a decrease in T_a, suggesting that GB segregation makes dislocation emission from GBs difficult. It should be noted that the driving force for grain boundary segregation due to the atomic-size differences is very small; hence, grain boundary segregation occurs at very low temperatures in the simplified virtual HEA models with the same chemical bonding energies between different elements. Although the segregation temperature may increase when the difference of chemical bonding energies are taken into account, it becomes impossible to distinguish whether the effect of grain boundary segregation on dislocation emission is due to grain boundary free volume or chemical bonding forces. Therefore, in the next paragraph, we will consider the effect of grain boundary segregation on dislocation emission in the virtual HEA models focused on the grain boundary free volume rather than the segregation temperature, which is affected by a variety of factors.

Figure 8 shows the relationship between the dislocation emission stress and the GB free volume impacted by the GB segregation in all the HEAs analyzed in this study. These are the main results of this study. The stress, σ_{dis}, and the free volume, V_{GB}, are normalized by the values for the random HEAs, $(\sigma_{dis})_{rnd}$ and $(V_{GB})_{rnd}$, respectively. Based on this definition, the stress–GB free volume relations in the random HEAs are all plotted on point (1, 1); therefore, we draw a fitting curve through the point to represent the trend of the stress–GB free volume relation in all the HEAs. We can confirm the increasing trend of the dislocation emission stress with a decrease in the GB free volume in both tensile/compressive load tests. As shown in Fig. 6, the GB free volume decreases with the GB segregation. This suggests that the GB segregation hinders the dislocation emission from the GBs in the HEAs. The fact that the CRSS required for dislocation emission from a GB with the same structure can be changed by adjusting only the size of the atoms constituting the GB reveals how the free volume at the GB affects the GB-mediated plastic deformation. Consequently, the strength of HEAs can be controlled by adjusting the degree of GB segregation.

IV. DISCUSSION

In the previous section, we stated that the stress required for dislocation emission from GBs in the HEAs increases with the degree of GB segregation. This relation is strongly related to the decrease in the GB free volume. Here, we discuss the effects of GB segregation on the mechanical properties of the HEAs, focusing on the homogenization of deformation and the activated slip systems.

A. Homogenization of local deformation due to grain boundary segregation

Here, we investigate the effects of the atomic-size difference and GB segregation on the mechanical field of HEAs

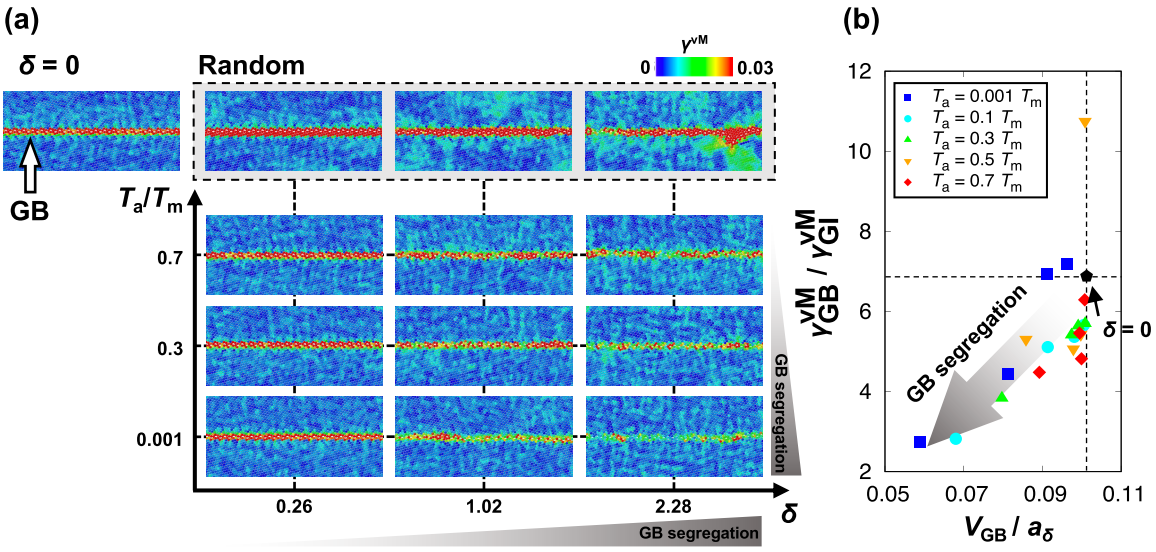

FIG. 9. (a) Atomic structures colored according to the atomic von Mises strain [69], γ^{vM}, around the $\Sigma 13$ boundaries in random HEAs and annealed HEAs at $T_a = 0.001\ T_m$, $0.3\ T_m$, and $0.7\ T_m$ at a tensile strain of 0.05. (b) Quantification of the localization of atomic-scale deformation using $\gamma^{\mathrm{vM}}_{\mathrm{GB}}/\gamma^{\mathrm{vM}}_{\mathrm{GI}}$, where $\gamma^{\mathrm{vM}}_{\mathrm{GB}}$ and $\gamma^{\mathrm{vM}}_{\mathrm{GI}}$ are the averaged von Mises strains over the GB regions (CSP > 0.3) and the grain interior regions (CSP $\leqslant 0.3$), respectively. The difference in strain magnitude between the grain boundary and the grain interior is remarkable in the single-element system ($\delta = 0$) and random HEAs because of the strain concentration at the grain boundary, while in annealed HEAs, the difference is smaller as the annealing temperature T_a decreases or the atomic size difference increases.

by comparing the strain fields during deformation in random HEAs and annealed HEAs.

Figure 9(a) shows the distribution of the atomic von Mises strain [68], γ^{vM} for each atom in the random HEAs and annealed HEAs at a tensile strain of 0.05 around the $\Sigma 13$ boundaries. For the HEAs without GB segregation, which are random HEAs, the atomic strain is concentrated near the GBs for all HEAs. This localization of the strain near the GBs during deformation can be understood by assuming that the local deformation originates from the GBs because the GBs are structurally unstable regions with higher energies than those of the grain interiors. However, the atomic strain near the GBs decreases with the annealing temperatures. The trend is more pronounced for HEAs with large δ, such as $\delta = 1.02$ and 2.28. This indicates that the deformation localization at the GBs, which could be the starting point of fracture, is suppressed in the HEAs with high degrees of GB segregation because the GBs are energetically stabilized by the decrease in the GB free volume (Fig. 3).

Figure 9(b) shows a quantitative representation of the suppression of the deformation localization in the GB regions, as described above, for the single-element materials ($\delta = 0$) and the annealed HEAs at T_a with the $\Sigma 13$ boundaries. Here, we calculate the average atomic strain, $\gamma^{\mathrm{vM}}_{\mathrm{GB}}$ in the GB regions (CSP > 0.3) relative to the average atomic strain $\gamma^{\mathrm{vM}}_{\mathrm{GI}}$ in the grain interiors (CSP $\leqslant 0.3$) as an index of the localization of the deformation in the GB region. The larger the value of $\gamma^{\mathrm{vM}}_{\mathrm{GB}}/\gamma^{\mathrm{vM}}_{\mathrm{GI}}$, the more localized the deformation in the GB regions. As the normalized free volume V_{GB}/a_δ decreases, $\gamma^{\mathrm{vM}}_{\mathrm{GB}}/\gamma^{\mathrm{vM}}_{\mathrm{GI}}$ tends to decrease, and the decrease in the free volume is correlated with the degree of GB segregation. This indicates that GB segregation decreases the free volume at the GBs and suppresses the localization of atomic strain near the GBs, resulting in homogeneous deformation in the whole system. In other words, in the HEAs with GB segregation, in addition to the increase in the CRSS for the dislocation emission from GBs, which results in improved strength, the suppression of localized deformation at GBs could prevent intergranular fracture and improve fracture toughness and ductility. As a result, it can be understood that GB segregation has the potential to increase the strength and ductility of HEAs.

B. Influence of grain boundary segregation on the active slip system

In the two-dimensional HEAs, the GB free volume is reduced by GB segregation (Fig. 6) and the GB structure also changes slightly, which may change the GB structure dependence of the dislocation emission from the GBs. If the dependence on the GB structure is weakened, dislocations can be emitted from any GB at a certain CRSS. In other words, HEAs may exhibit mechanically isotropic properties attributed to the GB segregation. In this section, we focus on the GBs with low-Σ values: the $\Sigma 21$, $\Sigma 13$, $\Sigma 7$, and $\Sigma 19$ boundaries, and we discuss the GB structure and slip systems in the dislocation emission from the GBs in HEAs based on the knowledge obtained from the analysis of the single-element materials ($\delta = 0$). The detailed analysis of the slip systems for the dislocation emission from the GBs in the single-element materials is shown in Appendix.

First, we consider the cases of the $\Sigma 13$ and $\Sigma 7$ boundaries. Figure 10 shows the dislocation emission from the $\Sigma 13$ and $\Sigma 7$ boundaries during (a) tensile and (b) compressive load tests in the annealed HEAs at $T_a = 0.5\ T_m$. The atomic colors represent the magnitude of the atomic von Mises strain [68], $\gamma^{\mathrm{vM}}_{\mathrm{GB}}$. The highlighted GBs indicate those where dislocation emission occurs because of the activation of the slip systems with the largest SF. For the $\Sigma 7$ boundary in $\delta = 0$, the

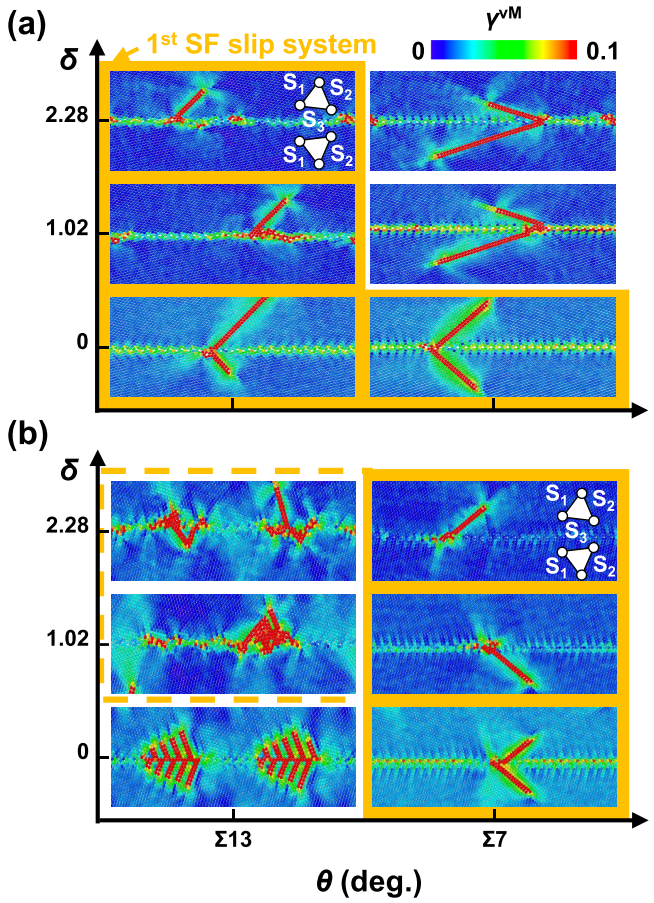

FIG. 10. Dislocation emission from the Σ13 and Σ7 boundaries in the annealed HEAs at $T_a = 0.5\,T_m$ during the (a) tensile and (b) compressive load tests. Atoms are colored according to the atomic von Mises strain [68], γ^{vM}. The dislocation emission with the largest SF slip system is highlighted in orange.

activated slip systems for both tensile and compressive load tests are the S_1 slip systems with the largest SF. Conversely, for the Σ13 boundary in $\delta = 0$, the activated slip system for the tensile load test is the S_1 slip system with the largest SF, although the activated slip system for the compressive load test is the S_2 slip system with the second largest SF. As shown in the Appendix, all activated slip systems utilize the Burgers vector for the GB dislocation at the structural unit. Therefore the CRSS of the activated S_2 slip system under compressive deformation in the Σ13 boundary can be smaller than that of the S_1 system with the largest SF, which cannot utilize the Burgers vector for the GB dislocation. For the HEA models with $\delta \neq 0$, it is confirmed that the activated slip systems can change depending on the type of GB and the loading direction. For the tensile deformation of the Σ7 boundary, the activated slip system changes from S_1 with the largest SF to S_3 with the second largest SF, and for the compressive deformation of the Σ13 boundary, the activated slip system changes from S_2 to multiple slip systems. The result indicates that the relative ability of the dislocation source for each slip system changes due to the GB segregation in the HEA models.

Next, to quantitatively evaluate the difference in the activated slip systems between the HEAs ($\delta \neq 0$) and

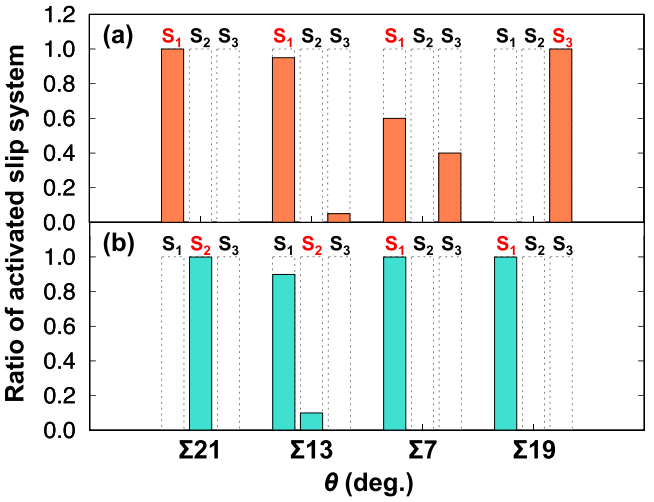

FIG. 11. Activated slip system, S_m, for the dislocation emission from the Σ21, Σ13, Σ7, and Σ19 boundaries in the annealed HEAs during the (a) tensile and (b) compressive load tests, respectively. The slip systems activated at $\delta = 0$ are highlighted in red. In the annealed HEAs, the same slip system at $\delta = 0$ tends to be activated, except for those of the Σ13 boundaries during the compressive load tests.

single-element materials ($\delta = 0$), Fig. 11 shows the percentage of the slip systems activated by (a) tensile and (b) compressive load tests for the various annealed HEAs at different δ and T_a (20 cases for each GB). The slip systems shown in red are those activated in the single-element materials, and the S_1 slip system has the largest SF in all cases. Although the notable slip-system changes associated with high-entropy alloying are confirmed in the cases of the Σ7 boundary under tensile deformation and the Σ13 boundary under compression, as shown in the previous paragraph, in most cases, the ability to realize dislocation emission due to GB structure is retained even when the GB free volume is significantly decreased by the GB segregation. This suggests that the GBs in HEAs can be mechanically stabilized by GB segregation without changing the geometrical characteristics of the GB structure. Consequently, exploiting the contribution of GB segregation, it is possible to realize excellent mechanical properties in HEAs by controlling the activated slip system through the design of the GB structure as in ultrafine-grained and nanocrystalline materials [27,34].

C. Extendability to three-dimensional realistic HEAs

The results discussed in the present study are obtained in the two-dimensional virtual HEAs considering only atomic-size difference between constituent elements, which have fundamental differences from three-dimensional HEAs due to the dimensionality. Nevertheless, the results indicate some essential features that can be independent of the dimensionality of the systems as described below. In this section, based on the common and uncommon features between two- and three-dimensional systems, we discuss what phenomena caused in the two-dimensional HEAs can be extended to three-dimensional ones.

The results from the two-dimensional HEAs potentially extendable to three-dimensional ones are as follows.

(1) GB segregation in the two-dimensional HEAs can be caused only by the atomic-size difference as a driving force (Sec. III 1 2). However, the driving force is small and only occurs at very low temperatures. In order for GB segregation to occur at temperatures where it has been observed in actual three-dimensional HEAs (i.e., temperatures at which sufficient diffusion phenomena can occur), other factors are necessary. One of the promising candidates is the chemical binding energy between different elements, which is not considered in the two-dimensional HEAs used in this study.

(2) The two-dimensional tilt GB structure can be expressed by a combination of structural units as well as a three-dimensional tilt GB structure (Fig. 2), and dislocation emission from GBs is strongly attributed to the GB dislocation component contained in the structural units [41]. This commonality suggests that the effect of GB segregation on dislocation emission from GBs obtained in two-dimensional HEAs can be applied to realistic three-dimensional ones.

(3) GB segregation energetically and geometrically stabilizes the GB and thereby suppresses the localization of deformation in the vicinity of the GB when an external force is applied, resulting in homogenization of the deformation (Sec. IV 1). Lattice distortion due to the atomic-size difference within the grain interior is kept remained, so the strength of the GB can be increased while maintaining the strength of the grain interior. This can be regarded as an unique phenomenon to HEAs.

On the other hand, there are many phenomena caused in actual three-dimensional HEAs that cannot be represented by the two-dimensional ones, among which the following are particularly important and require three-dimensional modeling: (a) the number of slip systems that can be activated by the two-dimensional HEAs is smaller than that of actual three-dimensional ones. Therefore the variety of dislocation emission phenomena from GBs is limited compared to three-dimensional HEAs. In three-dimensional systems, GBs are planar defects, and GB segregation is distributed two-dimensionally at the GB [69]. The free volume also shows a two-dimensional spatial distribution, and the activated slip system is not limited to dislocations parallel to the tilt axis, but various dislocations can be activated. (b) The two-dimensional HEAs used in this study cannot represent any extended dislocations, so the dislocation emission from GBs are all perfect dislocations, unlike in actual three-dimensional HEAs. The width of stacking faults generated by extended dislocations is relevent to the ability of dislocation glide such as cross slip; hence, the plastic deformation behavior in three-dimensional HEAs should be different from the two-dimensional ones. (c) In the two-dimensional HEAs, the dislocation shape is a straight line, but the dislocation in three-dimensional systems can be bent. In other words, dislocations are emitted from GBs by forming dislocation loops. Since the size of the dislocation loop is related to the activation volume, the phenomenon of dislocation emission from the GB has a temperature dependence that cannot be described by a two-dimensional model. Furthermore, GB segregation may affect the formation and the size of dislocation loops, in which case the temperature dependence of the mechanical properties of HEAs may change due to GB segregation.

The elucidation of these phenomena specific to three-dimensional HEAs will be conducted in our future work.

V. CONCLUSION

In this study, through atomic simulations, we systematically investigated the effects of GB segregation due to atomic-size differences on the dislocation emission from GBs in HEAs. To focus on the effect of the atomic-size difference on the GB segregation, ignoring the influence of chemical interaction forces, virtual quinary HEA models, wherein the bonding energies among all the atoms are equivalent and only the atomic sizes of the elements are different, were employed. The results are as follows.

(1) The GB segregation occurs due to the atomic-size difference in the virtual HEA models with the same chemical binding energies between different elements at very lower temperatures. However, the driving force for GB segregation due to the atomic-size differences is very small and the other factors, such as mixing enthalpy related to the chemical bonding energies between different elements, are necessary for GB segregation at higher temperatures to be feasible in actual HEAs.

(2) The GB free volume in the HEAs reduced significantly due to the GB segregation as the constituent elements in the HEAs had comparatively large atomic-size differences.

(3) The stress required for dislocation emission from the GBs increased with a decrease in the GB free volume, which hindered the dislocation emission from the GBs.

(4) In the annealed HEAs in which GB segregation occurred, the grain-size-scale heterogeneity of the mechanical fields between the grain interiors and their boundaries was reduced, whereas the geometrical characteristics of the GBs, such as the GB structural units, were retained after the annealing.

Our study showed that the grain-size-scale heterogeneity of the mechanical field between the grains and GBs in HEAs was reduced by GB segregation, caused by the atomic-size differences among the constituent elements, accounting for the unique mechanical properties of HEAs. We hope that our study plays a meaningful role in the creation of HEAs with unique properties and in understanding the associated mechanisms.

ACKNOWLEDGMENTS

This work was supported by JSPS KAKENHI Grants No. JP18H05453, No. JP21H00142, and No. JP21J21395.

APPENDIX: ACTIVE SLIP SYSTEM IN SINGLE-ELEMENT MATERIALS

In this Appendix, we describe the relationship between slip systems of dislocations emitted from GBs and GB structure using single-element systems ($\delta = 0$). These results are the basis of slip-system analysis of dislocations from GBs in HEAs.

In the two-dimensional bicrystals analyzed in this study, three kinds of slip systems could be activated. The black

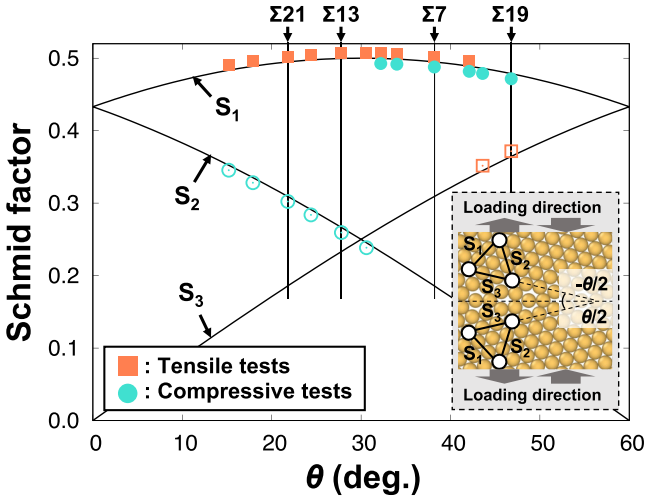

FIG. 12. Schmid factors (SFs) of three kinds of slip systems, $S_m m = 1,\ 2,$ and 3, as a function of the misorientation angle θ. The SFs are represented with solid (open) symbols when the largest SF slip system activates (does not activate) in single-element systems ($\delta = 0$).

lines in Fig. 12 show the SFs of each slip system, S_m ($m = 1,\ 2,$ and 3) as a function of the GB misorientation angle θ. The SFs of the activated slip systems during the tensile (compressive) load tests are plotted on the black lines in solid square (circle) symbols for the largest SF slip systems and in open square (circle) symbols for the other slip systems. When applying tensile load, the slip systems with the largest SF, S_1, are activated at the GBs with $\theta < 43.6°$, whereas those with the second largest SF, S_3, are activated at the GBs with $\theta \geqslant 43.6°$, Contrarily, when applying compressive load, the slip systems with the largest SF, S_1 activate at the GBs with $\theta \geqslant 32.2°$, whereas those with the second largest or the smallest SF, S_2, are activated at the GBs with $\theta < 32.2°$ Notably, when the largest SF slip systems do not activate, the GB structure according to its misorientation angle can promote the activation of the slip systems with comparatively low SFs from the GBs [25,39–41]. From the SF analyses, we can classify the GBs into three types: [GB–1] the largest SF slip systems are activated in both the tensile and compressive load tests, [GB–2] the largest SF slip systems are activated in only the tensile load tests, and [GB–3] the largest SF slip systems are activated in only the compressive load tests. In this Appendix, we investigate the roles of the GB structure in the dislocation emission from the three types of GBs using four kinds of GBs with low-Σ values; Σ7 as GB–1, Σ13 and Σ21 as GB–2, and Σ19 as GB–3.

Figures 13(a)–13(d) show the schematics of the dislocation emission from the four kinds of GBs at $\delta = 0$ during tensile/compressive load tests. The dislocations from the GBs during tensile and compressive load are colored in orange and blue, respectively. We define the GB dislocations by deter-

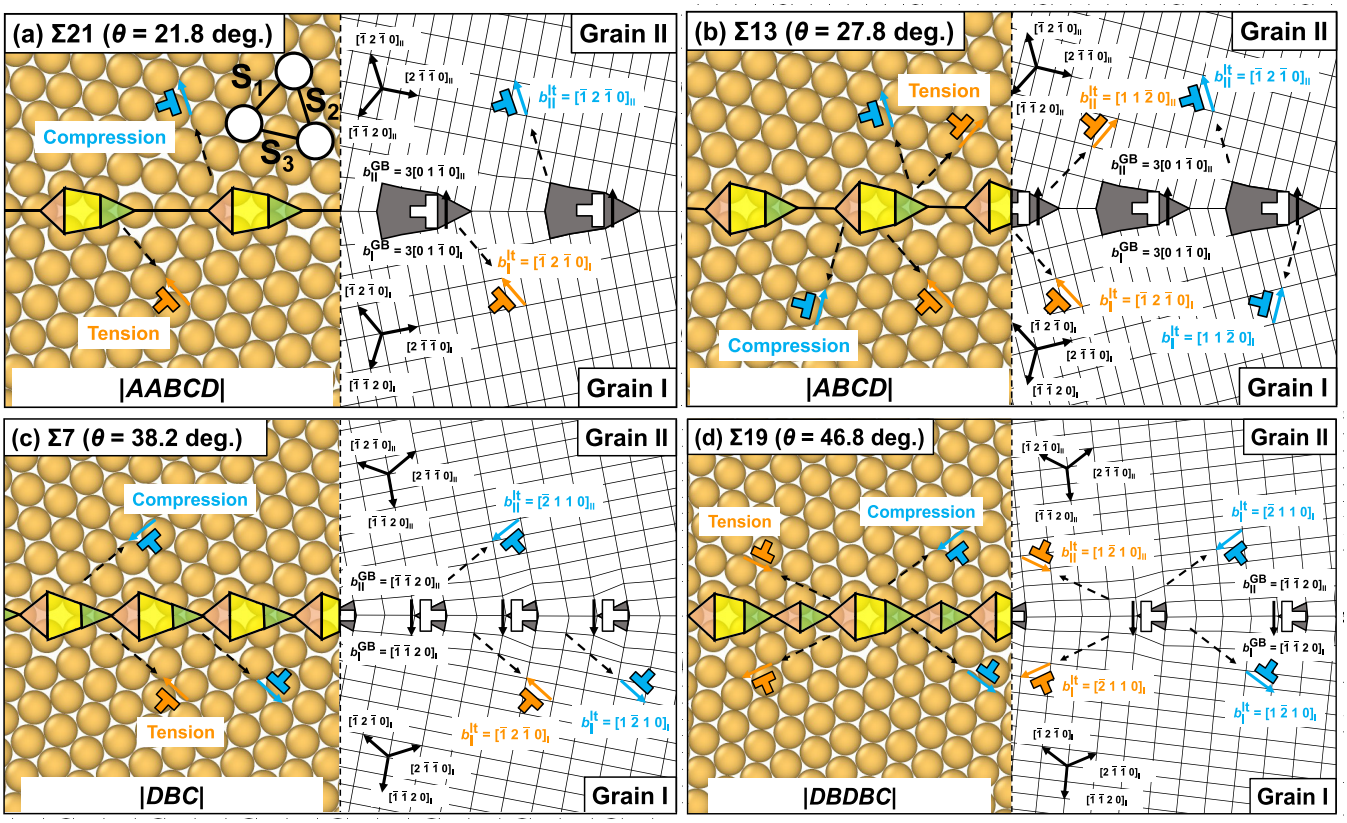

FIG. 13. GB structure of the (a) Σ21, (b) Σ13, (c) Σ7, and (d) Σ19 boundaries represented by the *A*, *B*, *C*, and *D* GB structural units and DSC lattices. The DSC lattice described in (a) Σ21 and (b) Σ13 GB is from that at $\theta = 0°$, and the DSC lattice described in (c) Σ7 and (d) Σ19 is from that at $\theta = 60°$ as a reference, respectively. The dislocations colored orange and blue are emitted from the GBs during tensile and compressive load tests, respectively. GB dislocations exit in the GB regions colored gray.

mining a referenced DSC lattice for each GB: a DSC lattice at $\theta = 0^\circ$ for the $\Sigma 21$ and $\Sigma 13$ boundaries with small θ, and a DSC lattice at $\theta = 60^\circ$ for the $\Sigma 7$ and $\Sigma 19$ boundaries with large θ. The DSC lattice analyses revealed that the magnitude of the Burgers vector for the GB dislocation in the gray region shown in Fig. 13 can be expressed in the units of the DSC lattice. Note that there are two GB dislocations within the gray region in the $\Sigma 21$ and $\Sigma 13$ boundaries. Since the grains in this study have triangular lattices with six-fold rotational symmetry, the coordinate systems of each grain, I and II, the Burgers vector for the slip systems, S_m, of the lattice dislocations, $\boldsymbol{b}_{\mathrm{I}}^{S_m}$, $\boldsymbol{b}_{\mathrm{II}}^{S_m}$, and the Burgers vector for the GB dislocations, $\boldsymbol{b}_{\mathrm{I}}^{\mathrm{GB}}$, $\boldsymbol{b}_{\mathrm{II}}^{\mathrm{GB}}$, can be conveniently represented with the Miller-Bravais index, which expresses crystallographic information of hexagonal crystals. For example, the GB dislocation in the $\Sigma 21$ boundary in the coordinate system of Grain I is represented by $\boldsymbol{b}_{\mathrm{I}}^{\mathrm{GB}} = 3[0\ 1\ \bar{1}\ 0]_{\mathrm{I}}$.

First, we focus on the dislocation emission from the GBs during the tensile load tests. The largest SF slip system is activated in the $\Sigma 21$, $\Sigma 13$ (GB–2), and $\Sigma 7$ boundaries (GB–1), whereas the second largest SF slip system is activated in the $\Sigma 19$ boundary (GB–3). The dislocations emitted from the $\Sigma 21$, $\Sigma 13$, and $\Sigma 19$ boundaries can utilize the components of the Burgers vectors of the GB dislocations. For example, the residual Burgers vector after dislocation emission from the $\Sigma 21$ boundary to Grain I is as follows:

$$\begin{aligned}\boldsymbol{b}_{\mathrm{I}}^{\mathrm{res}} &= \boldsymbol{b}_{\mathrm{I}}^{\mathrm{GB}} - \boldsymbol{b}_{\mathrm{I}}^{S_1} \\ &= 3[0\ 1\ \bar{1}\ 0]_{\mathrm{I}} - [\bar{1}\ 2\ \bar{1}\ 0]_{\mathrm{I}} \\ &= [1\ 1\ \bar{2}\ 0]_{\mathrm{I}}. \end{aligned} \tag{A1}$$

The magnitude of the residual Burgers vector, $|\boldsymbol{b}_{\mathrm{I}}^{\mathrm{res}}|$, is $1/\sqrt{3}$ of the Burgers vector for the GB dislocations, $|\boldsymbol{b}_{\mathrm{I}}^{\mathrm{GB}}|$; therefore, the lattice misfit due to the existence of the GB dislocations is partly relaxed, and the GBs are structurally stabilized. In the $\Sigma 13$ and $\Sigma 19$ boundaries, each GB dislocation completely decomposes into two lattice dislocations, $\boldsymbol{b}_{\mathrm{I}}^{S_m}$ for Grain I and $\boldsymbol{b}_{\mathrm{II}}^{S_m}$ for Grain II, and the decomposed lattice dislocations are emitted almost simultaneously. Therefore no Burgers vector remains at the GBs after the dislocation emission described in Eqs. (A2) and (A3) for each GB. Finally, the dislocation emission from the GBs utilizing the GB dislocation can stabilize the GB structure, indicating that this type of GBs can act as effective dislocation sources.

$$\begin{aligned}\boldsymbol{b}_{\mathrm{I}}^{\mathrm{res}} &= \boldsymbol{b}_{\mathrm{I}}^{\mathrm{GB}} - \boldsymbol{b}_{\mathrm{I}}^{S_1} - \boldsymbol{b}_{\mathrm{II}}^{S_1} \\ &= 3[0\ 1\ \bar{1}\ 0]_{\mathrm{I}} - [\bar{1}\ 2\ \bar{1}\ 0]_{\mathrm{I}} - [1\ 1\ \bar{2}\ 0]_{\mathrm{II}} \\ &= 3[0\ 1\ \bar{1}\ 0]_{\mathrm{I}} - [\bar{1}\ 2\ \bar{1}\ 0]_{\mathrm{I}} - [1\ 1\ \bar{2}\ 0]_{\mathrm{I}} \\ &= [0\ 0\ 0\ 0]_{\mathrm{I}}, \end{aligned} \tag{A2}$$

$$\begin{aligned}\boldsymbol{b}_{\mathrm{I}}^{\mathrm{res}} &= \boldsymbol{b}_{\mathrm{I}}^{\mathrm{GB}} - \boldsymbol{b}_{\mathrm{I}}^{S_3} - \boldsymbol{b}_{\mathrm{II}}^{S_3} \\ &= [\bar{1}\ \bar{1}\ 2\ 0]_{\mathrm{I}} - [\bar{2}\ 1\ 1\ 0]_{\mathrm{I}} - [1\ \bar{2}\ 1\ 0]_{\mathrm{II}} \\ &= [\bar{1}\ \bar{1}\ 2\ 0]_{\mathrm{I}} - [\bar{2}\ 1\ 1\ 0]_{\mathrm{I}} - [1\ \bar{2}\ 1\ 0]_{\mathrm{I}} \\ &= [0\ 0\ 0\ 0]_{\mathrm{I}}. \end{aligned} \tag{A3}$$

Notably, the activated slip system S_3 from the $\Sigma 19$ boundary is not the largest SF slip system, S_1. This can be achieved by ensuring that the CRSS of S_3, which uses the Burgers vector for the GB dislocation, is lower than the S_1 slip system with the largest SF.

Next, we focus on the dislocation emission from the GBs during the compressive load tests. The largest SF slip system, S_1, is activated in the $\Sigma 7$ and $\Sigma 19$ boundaries, whereas the second largest or the smallest SF slip system, S_2, is activated in the $\Sigma 21$ and $\Sigma 13$ boundaries for the dislocation emission. The dislocation emission using the Burgers vector component of the GB dislocations occurs at any of the four kinds of GBs. For examples, after the dislocation emission into Grain I, the Burgers vectors described in Eq. (A4) for the $\Sigma 21$ boundary and in Eq. (A5) for the $\Sigma 7$ boundary remain at the GBs:

$$\begin{aligned}\boldsymbol{b}_{\mathrm{I}}^{\mathrm{res}} &= \boldsymbol{b}_{\mathrm{I}}^{\mathrm{GB}} - \boldsymbol{b}_{\mathrm{I}}^{S_2} \\ &= 3[0\ 1\ \bar{1}\ 0]_{\mathrm{I}} - [1\ 1\ \bar{2}\ 0]_{\mathrm{I}} \\ &= [\bar{1}\ 2\ \bar{1}\ 0]_{\mathrm{I}}, \end{aligned} \tag{A4}$$

$$\begin{aligned}\boldsymbol{b}_{\mathrm{I}}^{\mathrm{res}} &= \boldsymbol{b}_{\mathrm{I}}^{\mathrm{GB}} - \boldsymbol{b}_{\mathrm{I}}^{S_1} \\ &= [\bar{1}\ \bar{1}\ 2\ 0]_{\mathrm{I}} - [1\ \bar{2}\ 1\ 0]_{\mathrm{I}} \\ &= [\bar{2}\ 1\ 1\ 0]_{\mathrm{I}}. \end{aligned} \tag{A5}$$

The GB dislocations are emitted into each grain, I and II, after decomposing into two dislocations in the $\Sigma 13$ and $\Sigma 19$ boundaries; therefore, no Burgers vector remains at the GBs, as described in Eq. (A6) for the $\Sigma 13$ boundary and Eq. (A7) for the $\Sigma 19$ boundary:

$$\begin{aligned}\boldsymbol{b}_{\mathrm{I}}^{\mathrm{res}} &= \boldsymbol{b}_{\mathrm{I}}^{\mathrm{GB}} - \boldsymbol{b}_{\mathrm{I}}^{S_2} - \boldsymbol{b}_{\mathrm{II}}^{S_2} \\ &= 3[0\ 1\ \bar{1}\ 0]_{\mathrm{I}} - [1\ 1\ \bar{2}\ 0]_{\mathrm{I}} - [\bar{1}\ 2\ \bar{1}\ 0]_{\mathrm{II}} \\ &= 3[0\ 1\ \bar{1}\ 0]_{\mathrm{I}} - [1\ 1\ \bar{2}\ 0]_{\mathrm{I}} - [\bar{1}\ 2\ \bar{1}\ 0]_{\mathrm{I}} \\ &= [0\ 0\ 0\ 0]_{\mathrm{I}}, \end{aligned} \tag{A6}$$

$$\begin{aligned}\boldsymbol{b}_{\mathrm{I}}^{\mathrm{res}} &= \boldsymbol{b}_{\mathrm{I}}^{\mathrm{GB}} - \boldsymbol{b}_{\mathrm{I}}^{S_1} - \boldsymbol{b}_{\mathrm{II}}^{S_1} \\ &= [\bar{1}\ \bar{1}\ 2\ 0]_{\mathrm{I}} - [1\ \bar{2}\ 1\ 0]_{\mathrm{I}} - [\bar{2}\ 1\ 1\ 0]_{\mathrm{II}} \\ &= [\bar{1}\ \bar{1}\ 2\ 0]_{\mathrm{I}} - [1\ \bar{2}\ 1\ 0]_{\mathrm{I}} - [\bar{2}\ 1\ 1\ 0]_{\mathrm{I}} \\ &= [0\ 0\ 0\ 0]_{\mathrm{I}}. \end{aligned} \tag{A7}$$

As shown above, not only the SFs of the activated slip systems but also those of the unique GB structural units depending on the GB misorientation angle have a significant impact on the dislocation emission from GBs in a single-element system.

[1] B. Cantor, I. T. H. Chang, P. Knight, and A. J. B. Vincent, Microstructural development in equiatomic multicomponent alloys, Mater. Sci. Eng., A **375–377**, 213 (2004).

[2] J. W. Yeh, S. K. Chen, S. J. Lin, J. Y. Gan, T. S. Chin, T. T. Shun, C. H. Tsau, and S. Y. Chang, Nanostructured high-entropy alloys with multiple principal elements: Novel

alloy design concepts and outcomes, Adv. Eng. Mater. **6**, 299 (2004).

[3] B. Gludovatz, A. Hohenwarter, D. Catoor, E. H. Chang, E. P. George, and R. O. Ritchie, A fracture-resistant high-entropy alloy for cryogenic applications, Science **345**, 1153 (2014).

[4] Y. Deng, C. C. Tasan, K. G. Pradeep, H. Springer, A. Kostka, and D. Raabe, Design of a twinning-induced plasticity high entropy alloy, Acta Mater. **94**, 124 (2015).

[5] Z. Li, K. Pradeep, Y. Deng, D. Raabe, and C. Tasan, Metastable high-entropy dual-phase alloys overcome the strength-ductility trade-off, Nature (London) **534**, 227 (2016).

[6] O. N. Senkov, G. B. Wilks, J. M. Scott, and D. B. Miracle, Mechanical properties of $Nb_{25}Mo_{25}Ta_{25}W_{25}$ and $V_{20}Nb_{20}Mo_{20}Ta_{20}W_{20}$ refractory high entropy alloys, Intermetallics **19**, 698 (2011).

[7] C.-C. Juan, M.-H. Tsai, C.-W. Tsai, C.-M. Lin, W.-R. Wang, C.-C. Yang, S.-K. Chen, S.-J. Lin, and J.-W. Yeh, Enhanced mechanical properties of HfMoTaTiZr and HfMoNbTaTiZr refractory high-entropy alloys, Intermetallics **62**, 76 (2015).

[8] M. A. Hemphill, T. Yuan, G. Y. Wang, J. W. Yeh, C. W. Tsai, A. Chuang, and P. K. Liaw, Fatigue behavior of $Al_{0.5}$CoCrCuFeNi high entropy alloys, Acta Mater. **60**, 5723 (2012).

[9] K. Lu, A. Chauhan, M. Walter, A. S. Tirunilai, M. Schneider, G. Laplanche, J. Freudenberger, A. Kauffmann, M. Heilmaier, and J. Aktaa, Superior low-cycle fatigue properties of CoCrNi compared to CoCrFeMnNi, Scr. Mater. **194**, 113667 (2021).

[10] Y. F. Ye, Q. Wang, J. Lu, C. T. Liu, and Y. Yang, High-entropy alloy: challenges and prospects, Mater. Today **19**, 349 (2016).

[11] D. B. Miracle and O. N. Senkov, A critical review of high entropy alloys and related concepts, Acta Mater. **122**, 448 (2017).

[12] H. Inui, K. Kishida, and Z. Chen, Recent progress in our understanding of phase stability, atomic structures and mechanical and functional properties of high-entropy alloys, Mater. Trans. **63**, 394 (2022).

[13] J. W. Yeh, Recent Progress in High-entropy Alloys, Ann. Chim.: Sci. Mater. **31**, 633 (2006).

[14] I. Toda-Caraballo and P. E. J. Rivera-Diaz-del-Castillo, Modelling solid solution hardening in high entropy alloys, Acta Mater. **85**, 14 (2015).

[15] C. Varvenne, A. Luque, and W. A. Curtin, Theory of strengthening in fcc high entropy alloys, Acta Mater. **118**, 164 (2016).

[16] C. Varvenne, G. P. M. Leyson, M. Ghazisaeidi, and W. A. Curtin, Solute strengthening in random alloys, Acta Mater. **124**, 660 (2017).

[17] R. Pasianot and D. Farkas, Atomistic modeling of dislocations in a random quinary high-entropy alloy, Comput. Mater. Sci. **173**, 109366 (2020).

[18] D. Farkas, Grain boundary structure in high-entropy alloys, J. Mater. Sci. **55**, 9173 (2020).

[19] D. Farkas, Deformation behavior of a model high entropy alloy from atomistic simulations, Mater. Sci. Eng., A **812**, 141124 (2021).

[20] N. L. Okamoto, K. Yuge, K. Tanaka, H. Inui, and E. P. George, Atomic displacement in the CrMnFeCoNi high-entropy alloy — A scaling factor to predict solid solution strengthening, AIP Adv. **6**, 125008 (2016).

[21] H. S. Oh, D. Ma, G. P. Leyson, B. Grabowski, E. S. Park, F. Körmann, and D. Raabe, Lattice distortions in the FeCoNiCrMn high entropy alloy studied by theory and experiment, Entropy **18**, 321 (2016).

[22] D. Wolf, Structure-energy correlation for grain boundaries in F. C. C. metals-III. Symmetrical tilt boundaries, Acta Metall. Mater. **38**, 781 (1990).

[23] T. Uesugi and K. Higashi, First-principles calculation of grain boundary energy and grain boundary excess free volume in aluminum: role of grain boundary elastic energy, J. Mater. Sci. **46**, 4199 (2011).

[24] T. Frolov and Y. Mishin, Molecular dynamics modeling of self-diffusion along a triple junction, Phys. Rev. B **79**, 174110 (2009).

[25] M. A. Tschopp, G. J. Tucker, and D. L. McDowell, Structure and free volume of ⟨110⟩ symmetric tilt grain boundaries with the E structural unit, Acta Mater. **55**, 3959 (2007).

[26] H. Van Swygenhoven, Grain boundaries and dislocations, Science **296**, 66 (2002).

[27] T. Shimokawa and M. Tsuboi, Atomic-scale intergranular crack-tip plasticity in tilt grain boundaries acting as an effective dislocation source, Acta Mater. **87**, 233 (2015).

[28] K. G. Pradeep, N. Wanderka, P. Choi, J. Banhart, B. S. Murty, and D. Raabe, Atomic-scale compositional characterization of a nanocrystalline AlCrCuFeNiZn high-entropy alloy using atom probe tomography, Acta Mater. **61**, 4696 (2013).

[29] D. Raabe, M. Herbig, S. Sandlöbes, Y. Li, D. Tytko, M. Kuzmina, D. Ponge, and P.-P. Choi, Grain boundary segregation engineering in metallic alloys: A pathway to the design of interfaces, Curr. Opin. Solid State Mater. Sci. **18**, 253 (2014).

[30] Y. Zou, P. Okle, H. Yu, T. Sumigawa, T. Kitamura, S. Maiti, W. Steurer, and R. Spolenak, Fracture properties of a refractory high-entropy alloy: In situ micro-cantilever and atom probe tomography studies, Scr. Mater. **128**, 95 (2017).

[31] C. M. Barr II, J. E. Nathaniel II, K. A. Unocic, J. Liu, Y. Zhang, Y. Wang, and M. L. Taheri, Exploring radiation induced segregation mechanisms at grain boundaries in equiatomic CoCrFeNiMn high entropy alloy under heavy ion irradiation, Scr. Mater. **156**, 80 (2018).

[32] L. Li, Z. Li, A. Kwiatkowski da Silva, Z. Peng, H. Zhao, B. Gault, and D. Raabe, Segregation-driven grain boundary spinodal decomposition as a pathway for phase nucleation in a high-entropy alloy, Acta Mater. **178**, 1 (2019).

[33] L. Li, R. D. Kamachali, Z. Li, and Z. Zhang, Grain boundary energy effect on grain boundary segregation in an equiatomic high-entropy alloy, Phys. Rev. Mater. **4**, 053603 (2020).

[34] T. Shimokawa, T. Niiyama, T. Miyaki, M. Ikeda, and K. Higashida, A novel work hardening mechanism of nanoscale materials by grain boundary transformation, Acta Mater. **224**, 117536 (2022).

[35] P. Wynblatt and D. Chatain, Modeling grain boundary and surface segregation in multicomponent high-entropy alloys, Phys. Rev. Mater. **3**, 054004 (2019).

[36] D. Utt, A. Stukowski, and K. Albe, Grain boundary structure and mobility in high-entropy alloys: A comparative molecular dynamics study on a Σ11 symmetrical tilt grain boundary in face-centered cubic CuNiCoFe, Acta Mater. **186**, 11 (2020).

[37] K. Shiotani, T. Niiyama, and T. Shimokawa, Dislocation emission from grain boundaries in high-entropy alloys: Influence of atomic compositions at grain boundaries, Mater. Trans. **61**, 1272 (2020).

[38] X. G. Li, C. Chen, H. Zheng, Y. Zuo, and S. P. Ong, Complex strengthening mechanisms in the NbMoTaW multi-principal element alloy, npj Comput. Mater. **6**, 70 (2020).

[39] D. E. Spearot, M. A. Tschopp, K. I. Jacob, and D. L. McDowell, Tensile strength of ⟨100⟩ and ⟨110⟩ tilt bicrystal copper interfaces, Acta Mater. **55**, 705 (2007).

[40] D. E. Spearot, Evolution of the E structural unit during uniaxial and constrained tensile deformation, Mech. Res. Commun. **35**, 81 (2008).

[41] T. Shimokawa, Asymmetric ability of grain boundaries to generate dislocations under tensile or compressive loadings, Phys. Rev. B **82**, 174122 (2010).

[42] M. P. Allen and D. J. Tildesley, *Computer Simulation of Liquids* (Oxford University Press, New York, 1987).

[43] P. M. Morse, Diatomic molecules according to the wave mechanics. II. Vibrational levels, Phys. Rev. **34**, 57 (1929).

[44] W. M. Choi, Y. H. Jo, S. S. Sohn, S. Lee, and B. J. Lee, Understanding the physical metallurgy of the CoCrFeMnNi high-entropy alloy: An atomistic simulation study, npj Comput. Mater. **4**, 1 (2018).

[45] D. Farkas and A. Caro, Model interatomic potentials and lattice strain in a high-entropy alloy, J. Mater. Res. **33**, 3218 (2018).

[46] O. R. Deluigi, R. C. Pasianot, F. J. Valencia, A. Caro, D. Farkas, and E. M. Bringa, Simulations of primary damage in a High Entropy Alloy: Probing enhanced radiation resistance, Acta Mater. **213**, 116951 (2021).

[47] X. Huang, L. Liu, X. Duan, W. Liao, J. Huang, H. Sun, and C. Yu, Atomistic simulation of chemical short-range order in HfNbTaZr high entropy alloy based on a newly-developed interatomic potential, Mater. Des. **202**, 109560 (2021).

[48] R. Gröger, V. Vitek, and A. Dlouhy, Effective pair potential for random fcc CoCrFeMnNi alloys, Modell. Simul. Mater. Sci. Eng. **28**, 075006 (2020).

[49] S. Fang, X. Xiao, L. Xia, W. Li, and Y. Dong, Relationship between the widths of supercooled liquid regions and bond parameters of Mg-based bulk metallic glasses, J. Non-Cryst. Solids **321**, 120 (2003).

[50] L. A. Girifalco and V. G. Weizer, Application of the morse potential function to cubic metals, Phys. Rev. **114**, 687 (1959).

[51] P. C. Millett, R. P. Selvam, S. Bansal, and A. Saxena, Atomistic simulation of grain boundary energetics — Effects of dopants, Acta Mater. **53**, 3671 (2005).

[52] D. Udler and D. N. Seidman, Grain boundary and surface energies of fcc metals, Phys. Rev. B **54**, R11133(R) (1996).

[53] C. L. Kelchner, S. J. Plimpton, and J. C. Hamilton, Dislocation nucleation and defect structure during surface indentation, Phys. Rev. B **58**, 11085 (1998).

[54] J. D. Rittner and D. N. Seidman, ⟨110⟩ symmetric tilt grain-boundary sructures in fcc metals with low stacking-fault energies, Phys. Rev. B **54**, 6999 (1996).

[55] D. Wolf, Structure-energy correlation for grain boundaries in F. C. C. metals-I. Boundaries on the (111) and (100) planes, Acta Metall. **37**, 1983 (1989).

[56] D. Wolf, Correlation between the energy and structure of grain boundaries in b.c.c. metals I. symmetrical boundaries on the (110) and (100) planes, Philos. Mag. B **59**, 667 (1989).

[57] D. Wolf and S. Phillpot, Role of the densest lattice planes in the stability of crystalline interfaces: A computer simulation study, Mater. Sci. Eng., A **107**, 3 (1989).

[58] D. Wolf, Correlation between the energy and structure of grain boundaries in b.c.c. metals. II. Symmetrical tilt boundaries, Philos. Mag. A **62**, 447 (1990).

[59] D. Wolf, A broken-bond model for grain boundaries in facecentered cubic metals, J. Appl. Phys. **68**, 3221 (1990).

[60] Y. Hu and T. J. Rupert, Atomistic modeling of interfacial segregation and structural transitions in ternary alloys, J. Mater. Sci. **54**, 3975 (2019).

[61] M. Parrinello and A. Rahman, Crystal structure and pair potentials: A molecular-dynamics study, Phys. Rev. Lett. **45**, 1196 (1980).

[62] A. Stukowski, Visualization and analysis of atomistic simulation data with OVITO — the open visualization tool, Modell. Simul. Mater. Sci. Eng. **18**, 015012 (2010).

[63] D. Wolf, Structure-energy correlation for grain boundaries in f.c.c. metals-II. Boundaries on the (110) and (113) planes, Acta Metall. **37**, 2823 (1989).

[64] D. Wolf, Structure-energy correlation for grain boundaries in f.c.c. metals IV. Asymmetrical twist (general) boundaries, Acta Metall. Mater. **38**, 791 (1990).

[65] H. Sun and C. V. Singh, Temperature dependence of grain boundary excess free volume, Scr. Mater. **178**, 71 (2020).

[66] F. Cao, Y. Jiang, T. Hu, and D. Yin, Correlation of grain boundary extra free volume with vacancy and solute segregation at grain boundaries: A case study for Al, Philos. Mag. **98**, 464 (2018).

[67] C. H. Rycroft, Voro++: A three-dimensional Voronoi cell library in C++, Chaos **19**, 041111 (2009).

[68] F. Shimizu, S. Ogata, and J. Li, Theory of shear bonding in metallic glasses and molecular dynamics calculations, Mater. Trans. **48**, 2923 (2007).

[69] G. J. Tucker, M. A. Tschopp, and D. L. McDowell, Evolution of structure and free volume in symmetric tilt grain boundaries during dislocation nucleation, Acta Mater. **58**, 6464 (2010).